

Topological Phase Transition in Quantum Heat Engine Cycles

Mojde Fadaie,^{1,*} Elif Yunt,^{1,†} and Özgür E. Müstecaplıoğlu^{1,‡}

¹*Department of Physics, Koç University, 34450 Sarıyer, Istanbul TURKEY*

We explore signatures of a topological phase transition (TPT) in the work and efficiency of a quantum heat engine, which uses a single layer topological insulator, stanene, in an external electric field as a working substance. The magnitude of the electric field controls the trivial and topological insulator phases of the stanene. We investigate the effects of TPT in two types of thermodynamic cycles, with and without adiabatic stages. For the adiabatic case, we examine a quantum Otto cycle. We find that at the critical point of TPT both work and efficiency plots with respect to the strength of the electric field exhibit a kink. For a non-adiabatic case, we consider an idealized Stirling type cycle with two isothermal and two isoelectric processes. We find no signatures of the TPT unless a voltage bias is introduced to restrict the involved energy bands to the electronic manifold above the Fermi level. In this case, either above or below the critical point, both work and efficiency become zero depending on the relative magnitudes of the electric fields in the isoelectric stages.

I. INTRODUCTION

Heat engines are the practical motivations and significant outcomes of the field of thermodynamics, which led to high socioeconomic impact in the industrial revolutions [1]. In parallel with the social and industrial developments, list of the working substances in the heat engines has been grown since the steam engine in 18th century, and included three-level masers [2], cavity photons [3], spin systems [4], single atom [5], atomic clusters [6], optomechanical systems [7], superconducting resonators [8], Dirac particles [9, 10], graphene flake [11–13], black holes [14], and ultracold atoms [15]. Heat engines that are using working substances requiring quantum mechanical descriptions are called as quantum heat engines (QHEs), whose cycles [16] are studied under a quantum thermodynamical framework, which is an emerging and rapidly progressing field of research [16–20]. Experimental demonstrations of a single-atom heat engine [5] and QHEs with nitrogen-vacancy centers in diamond [21] and with cold Rb atoms [22] have been shown.

Typically the working system of the engine remains in a single-phase during a thermodynamic cycle. In practice, however, phase changes can happen during the engine operation and can enhance the efficiency. Power plants, for example, can be modeled by the Rankine cycle, which is based upon water-steam phase transition. Recently it has been argued that diverging fluctuations at a second order phase transitions can help to achieve Carnot efficiency in a quantum Otto engine [23]. More recently, it has been shown that a quantum phase transition of an interacting spin working system allows for reaching Carnot efficiency [24]. Inspired by these results, we ask if a topological phase transition (TPT) during a quantum engine cycle can have any significant effects on the efficiency. Furthermore, we explore if such effects can be used

to probe a TPT. In contrast to the ordinary QPTs, TPTs has no local order parameter associated with symmetry breaking. TPT is described by a bulk invariant (Chern number) which is an integer and changes to another integer at the TPT. In case of gap closing at the TPT, we expect that global nature of the work could capture the TPT qualitatively in certain cycles.

Usually, statistical work distribution measurements are studied in suddenly and infinitesimally quenched systems to examine phase transitions in quantum critical models [25]. Quench protocols bring the systems out of equilibrium and the work output is given by a probability distribution whose characteristic function can be related to the Loschmidt echo that can be determined in principle experimentally. It is shown that local quenches lead to edge singularities in the work distribution in a quantum critical system [26]. Our approach is on the other hand based upon a cyclic variation of a control parameter, instead of quenching, and to look for signatures of TPT in the work output of the cycle.

We specifically consider a 2D monolayer Stanene (Sn) as our working substance. Stanene is a counterpart of graphene for tin atoms [27–29] with low-buckled honeycomb geometry [30]. In contrast to graphene it has a larger spin-orbit coupling [31, 32], can host the quantum spin Hall effect at room temperature for dissipationless electric currents [27], and its band structure, in particular, Dirac cone band gap, can be controlled with an out-of-plane electric field such that it exhibits a TPT between two-dimensional trivial and topological insulator (2DTI) phases depending on the applied electric field [33–36]. 2D Sn has been fabricated recently by molecular beam epitaxy [37]. Studies of thermal properties of Sn is limited to thermoelectrics so far [38]. Its outstanding properties, on the other hand, make it also an ideal candidate for a working substance of a room temperature topological QHE. We note that using heat, instead of work, has been considered to detect dynamical phase transitions and Majorana modes recently [39]. It is proposed there that Floquet-Majorana phases can be used for QHEs or heat pumps. Our simple model here can be envisioned as the first step towards QHEs with more sophisticated

* mfadaei@ku.edu.tr

† eyunt@ku.edu.tr

‡ omustecap@ku.edu.tr

topological materials with TPTs.

By using an external electric field as the control parameter we consider adiabatic (specifically the Otto cycle) and non-adiabatic (specifically a Stirling type cycle as in Ref. [24]) thermodynamic cycles in which Sn undergoes a topological phase transition. We calculate the work output and efficiency of the cycles; determine and compare the signatures of the TPT in both types of cycles. We find out that the answer to our question for both cycles is positive, TPT of Sn can be probed by using work and efficiency of QHE cycles. Highly distinct characteristic behaviors are obtained below and above the critical point of TPT. Another advantage of Sn working substance is that the QHE with TPT can operate around room temperature without the need for large external electric fields. We briefly discuss how to implement the cycle in an experimental setting a graphene bilayer as a scaffold at the end of the manuscript.

This paper is organized as follows: We review the theory and TPT of Sn in Sec. II. The results and discussions are presented in Sec. III in two subsections where quantum Otto cycle case is presented in Sec. III A and non-adiabatic cycle case is presented in Sec. III B. In Sec. IV, a possible experimental realization is discussed. We conclude in Sec. V. The details of the calculations of the work output for both of the quantum thermodynamic cycles are given in the Appendices A and B.

II. WORKING SUBSTANCE

This section is a brief review of relevant properties of Sn for our QHE and TPT discussions. We consider a single layer of two-dimensional Sn in the xy -plane as the working substance for a QHE. An external electric field ε_z is applied in the z -direction, perpendicular to the atomic layer. The system is described by a second-nearest-neighbor tight-binding model given in Ref [29]

$$H = -t \sum_{\langle i,j \rangle \alpha} c_{i\alpha}^\dagger c_{j\alpha} + i \frac{\lambda_{\text{SO}}}{3\sqrt{3}} \sum_{\langle\langle i,j \rangle\rangle \alpha\beta} v_{ij} c_{i\alpha}^\dagger \sigma_{\alpha\beta}^z c_{j\beta} - i \frac{2\lambda_R}{3} \sum_{\langle\langle i,j \rangle\rangle \alpha\beta} \mu_{ij} c_{i\alpha}^\dagger (\vec{\sigma} \times \vec{d}_{ij}^0)_{\alpha\beta}^z c_{j\beta} + l \sum_{i\alpha} \zeta_i \varepsilon_z c_{i\alpha}^\dagger c_{i\alpha}. \quad (1)$$

The first term is the nearest-neighbor hopping term and t is the transfer energy. The sum is taken over all pairs $\langle i,j \rangle$ of the nearest neighboring sites, $c_{i\alpha}^\dagger$ and $c_{j\alpha}$ create and annihilate an electron with spin polarization α at site i , respectively. The second and third terms are the effective and intrinsic Rashba spin-orbit interactions with the corresponding coefficients λ_{SO} and λ_R , respectively. μ_{ij} and ζ_i are equal to ± 1 for two sublattices of Sn. $\vec{\sigma}$ denote the Pauli matrices; The coefficients v_{ij} are defined as

$$v_{ij} = \vec{d}_i \times \vec{d}_j / |\vec{d}_i \times \vec{d}_j| \quad (2)$$

where \vec{d}_i and \vec{d}_j are the two nearest bonds connecting the next-nearest neighbors \vec{d}_{ij} and $\vec{d}_{ij}^0 = \vec{d}_{ij} / |\vec{d}_{ij}|$. l is half of the perpendicular distance between two sublattices. The sum is taken over all pairs $\langle\langle i,j \rangle\rangle$ of the next-nearest neighbors. We note that the model describes other two-dimensional honeycomb structure as well [29, 40].

The low-energy effective Hamiltonian for stanene is derived from Eq. (1) around the K_η point in Ref. [29, 31] as

$$H_{s\eta} = \hbar v_f (\tau_x k_x - \eta k_y \tau_y) - \eta \lambda_{\text{SO}} \tau_z \sigma_z + l \varepsilon_z \tau_z, \quad (3)$$

where v_f is the Fermi velocity and $\tau_{x,y,z}$ are the Pauli matrices of the sublattice. Here, we ignore the Rashba term in Ref. [29], as we will consider the behavior of the bands exactly at the Dirac points where the Rashba term vanishes. The energy spectrum of Eq. (3) is found to be [29]

$$E_{s\eta}(k) = \pm \sqrt{\hbar^2 v_f^2 k^2 + (l \varepsilon_z - s \eta \lambda_{\text{SO}})^2}, \quad (4)$$

where $k = \sqrt{k_x^2 + k_y^2}$ and $s = \pm$ is the electron spin. There are in total four distinct energy eigenvalues, which are each four-fold degenerate due to the valley and spin degrees of freedom.

Low energy band structure of Sn at the vicinity of K point given by Eq. 4 shows that the energy gap $\Delta = 2|\lambda_{\text{SO}} - l \varepsilon_z|$ at $k = 0$ is finite at $\varepsilon_z = 0$; it decreases and closes at critical value ε_{cr} . The phase diagram of Sn with respect to the external electric field is shown in Fig. 1. The gap closing occurs at $\varepsilon_z = \pm \varepsilon_{cr}$. It is found that gap closing is associated with TPT such that for $|\varepsilon_z| < \varepsilon_{cr}$ Sn is a TI and for $|\varepsilon_z| > \varepsilon_{cr}$ it is a band insulator [29, 35, 36].

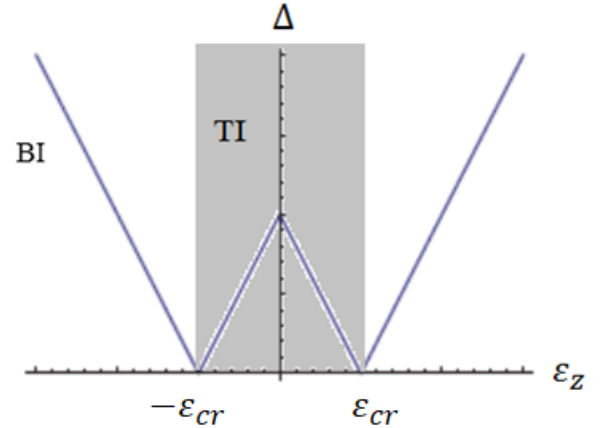


Figure 1. (Color Online) Variation of band gap Δ as a function of external electric field ε_z . The gap is closed at the critical points $\varepsilon_z = \pm \varepsilon_{cr}$. Band closing is associated with a topological phase change for Sn such that for $|\varepsilon_z| > \varepsilon_{cr}$ Sn is a band insulator (BI); while otherwise it is a topological insulator (TI).

III. RESULTS AND DISCUSSION

A. Quantum Otto Cycle

A quantum Otto cycle (QOC) consists of two isochoric and two adiabatic processes [16]. We consider a QOC with topological insulator as a working substance. The direction of the cycle is chosen such that net positive work is produced, as is depicted in Fig. 2. The four stages of the QOC are as follows:

- Stage 1 (A to B): This is a quantum isochoric process where the working substance in an external electric field, ε_h , with energy levels E_n^h is coupled to a hot bath at temperature T_h . At point B, the working substance reaches thermal equilibrium with the hot bath, and the occupation probability of each eigenstate becomes $P_n(T_h)$, while the energy levels remain the same. No work is done but heat Q_{in}

$$Q_{in} = \sum_n E_n^h [P_n(T_h) - P_n(T_c)] \quad (5)$$

is absorbed by the working substance during this process.

- Stage 2 (B to C): In this process, which is a quantum adiabatic process, the working substance is isolated from the heat bath and the electric field changes from ε_h to ε_c , where $\varepsilon_c < \varepsilon_h$. The energy levels change from E_n^h to E_n^c . The occupation probabilities do not change. Work is done but no heat is transferred.
- Stage 3 (C to D): The working substance is subject to a constant electric field, ε_c , and is coupled to a cold bath at temperature $T_c < T_h$. The occupation probabilities at the end of this stage are $P_n(T_c)$. Heat Q_{out}

$$Q_{out} = \sum_n E_n^c [P_n(T_c) - P_n(T_h)] \quad (6)$$

is ejected from the system. In Eq. 5 and Eq. 6, $P_n(T_i) = \exp(-\beta_i E_i^n) / Z_i$ with $i = h, c$, $\beta_i = k_B T_i$ where k_B is the Boltzmann constant. $Z_i = \sum_n \exp(-\beta_i E_i^n)$ is the partition function and n counts the energy eigenvalues of the system.

- Stage 4 (D to A): The system is separated from the cold bath and undergoes another quantum adiabatic process, as the electric field is changed from ε_c to ε_h . Energy levels change from E_n^c to E_n^h . The occupation probabilities remain the same. There is no heat transfer but work is done.

As the probability distribution remains invariant in the two quantum adiabatic processes, the entropy will remain invariant as well and no net heat is produced. Based on

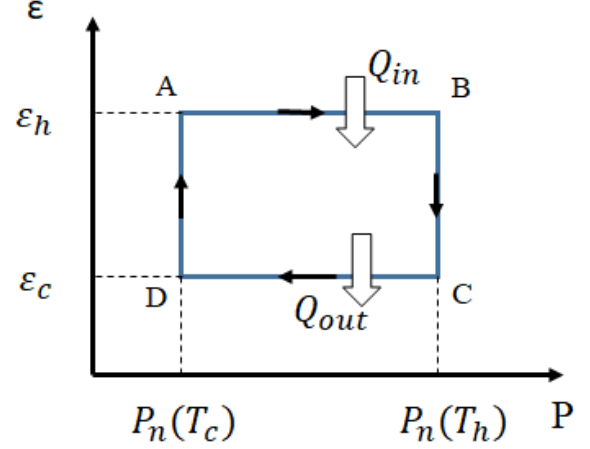


Figure 2. Quantum Otto cycle operating between a hot bath at temperature T_h and a cold bath at temperature T_c . It has of two isochoric (A to B and C to D) and adiabatic (B to C and D to A) processes for Sn under electric field ε_z . Q_{in} is the heat injected in the A-B stage, and Q_{out} is the heat ejected in the C-D stage. Electric field changes between ε_h and ε_c . Occupation probabilities P of an energy level E_n changes between $P_n(T_c)$ and $P_n(T_h)$.

this fact, the net work produced during a QOE cycle is given by

$$\begin{aligned} W_O &= Q_{in} + Q_{out} \\ &= \sum_n (E_n^h - E_n^c) [P_n(T_h) - P_n(T_c)] \end{aligned} \quad (7)$$

The efficiency of the heat engine is $\eta_O = W_O / Q_{in}$. Positive work condition requires $Q_{in} > -Q_{out}$, under which the system would operate as a heat engine.

Substituting Eq. 4 for $k = 0$ into Eq. (7) the net work is found to be

$$\begin{aligned} W_O &= 2(|\varepsilon_h - \lambda_{SO}| - |\varepsilon_c - \lambda_{SO}|) \times \\ &\quad \left(\frac{\sinh(\beta_c |\varepsilon_c - \lambda_{SO}|)}{Z_c} - \frac{\sinh(\beta_h |\varepsilon_h - \lambda_{SO}|)}{Z_h} \right) \\ &\quad + 2(\varepsilon_h - \varepsilon_c) \times \\ &\quad \left(\frac{\sinh(\beta_c (\varepsilon_c + \lambda_{SO}))}{Z_c} - \frac{\sinh(\beta_h (\varepsilon_h + \lambda_{SO}))}{Z_h} \right), \end{aligned} \quad (8)$$

where $Z_i = 8 \cosh(\beta_i |\varepsilon_i - \lambda_{SO}|) + 8 \cosh(\beta_i (\varepsilon_i + \lambda_{SO}))$ with $i = c, h$. The details of the calculations leading to (8) are in Appendix A.

We take typical values for the parameters of Sn TI model [31] where $\lambda_{SO} = 30$ meV and ε_h and ε_c are in the range 0 – 60 meV. We separately consider high and low temperature operation of the engine. For the high temperature case we take the temperatures of the hot and the cold baths as $T_h = 400$ K and $T_c = 300$ K, respectively; while for the low temperature case we assume $T_h = 100$ K and $T_c = 30$ K.

In Fig. 3 we show the electric potential domain of the positive work, $W_O > 0$, as the shaded region. The positive work region linearly expands with the increasing electric fields, except a semicircular region terminated by the critical points of TPT at $l_{\varepsilon_{cr}} = \lambda_{SO}$. Fig. 3 could also be plotted for the negative values of the electric fields. The result would be inversion of the positive work region in Fig. 3 with respect to the origin.

Exact values and behavior of the work output as a function of l_{ε_c} , for three representative values of l_{ε_h} , are plotted in Fig. 4. It shows a double peak profile. Zeros of the work function separate the regimes of the heat engine and heat pump or refrigerator operations of the system. The number of zeros can be deduced from Fig. 3 by the boundary of the shaded region. The critical point of TPT reveals itself as a kink in the curves at $l_{\varepsilon_c} = \lambda_{SO} = 30$ meV. As l_{ε_h} is decreased the kink moves up from negative to positive values, where the system operates as a heat engine.

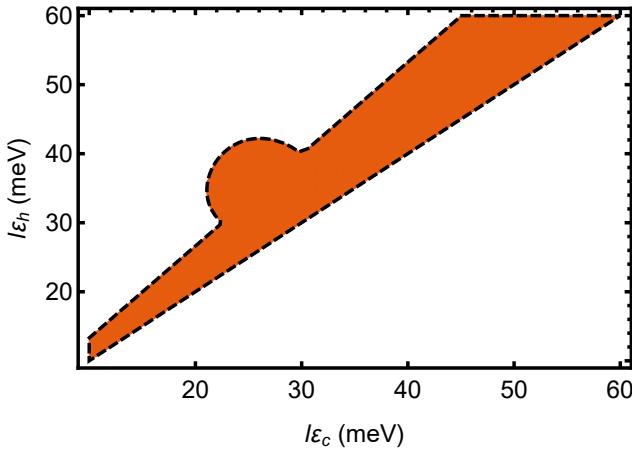


Figure 3. (Color Online) Domain of positive work in the space of external electric potentials at the cold and hot isochores l_{ε_c} and l_{ε_h} , respectively. Dashed lines separates the positive (shaded) and negative (white) work regions. The parameters are the spin-orbit coupling $\lambda_{SO} = 30$ meV, and the temperatures of the hot and the cold baths $T_h = 400$ K and $T_c = 300$ K, respectively.

The kink appears in the efficiency behavior as well, as shown in Fig. 5, where we take $l_{\varepsilon_h} = 35$ meV. Qualitatively similar behaviors are found for the low-temperature case. Fig. 6 indicates that the efficiency is higher for the low-temperature case.

Signatures of the TPT found in the positive work domain and in the behaviors of the work and efficiency with the applied electric fields can be challenging to observe in practice. The reason is that TPT is associated with the crossing of energy levels and hence the electric field variation must be infinitely slow towards the critical point in order to comply with the quantum adiabatic theorem during the adiabatic stages of the Otto cycle. One may avoid crossing the TPT point by taking $l_{\varepsilon_h}, l_{\varepsilon_c}$ at the same side of the critical point and look for qualitative

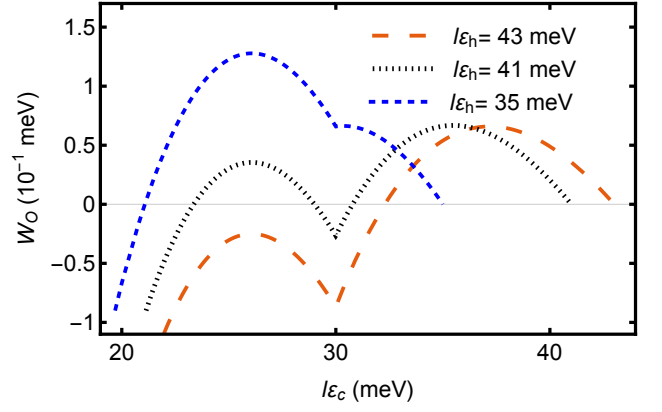


Figure 4. (Color Online) Work output, W_O of the quantum Otto cycle operating between the hot and cold bath temperatures $T_h = 400$ K and $T_c = 300$ K, respectively, as a function of the electric potential at the cold isochore l_{ε_c} for different values of the electric potential at the hot isochore $l_{\varepsilon_h} = 43$ meV (red long dashed), $l_{\varepsilon_h} = 41$ meV (black dotted), and $l_{\varepsilon_h} = 35$ meV (blue short dashed). SO coupling is $\lambda_{SO} = 30$ meV.

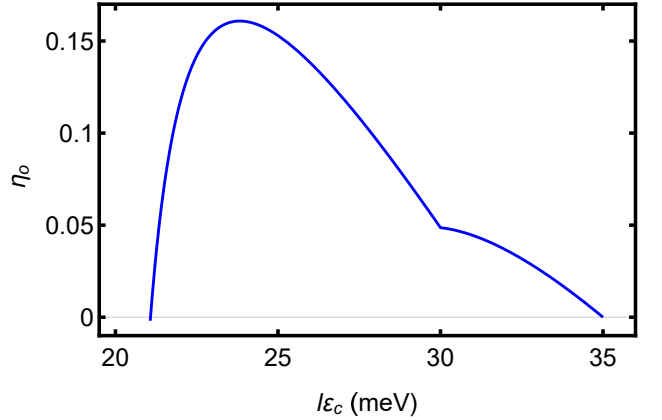


Figure 5. (Color Online) Efficiency η_{SO} of quantum Otto cycle for the electric potential at the hot isochore $l_{\varepsilon_h} = 35$ meV, spin-orbit coupling $\lambda_{SO} = 30$ meV, and the temperatures of the hot and the cold baths $T_h = 400$ K and $T_c = 300$ K, respectively.

changes in the behavior of work by varying the fields or introduce transitionless drives[41]. An easier alternative is to remove the adiabatic stages from the cycle completely. In the following subsection, we will consider a non-adiabatic cycle, which is used in Ref. [24] to explore signatures of a quantum phase transition.

B. Stirling Cycle

It is reported in Ref. [24] that signatures of a quantum phase transition, associated with a level closing, can be found in the work and efficiency of a thermodynamic cycle, which consists of two isothermal and two isomagnetic

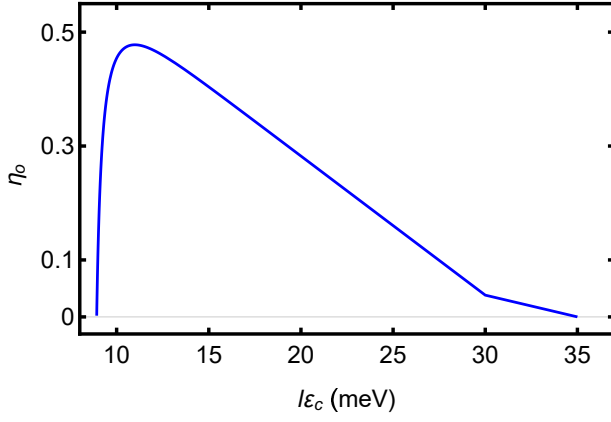


Figure 6. (Color Online) Efficiency η_{SO} of quantum Otto heat engine at low temperatures for the electric potential at the hot isochore $l\varepsilon_h = 35$ meV, spin-orbit coupling $\lambda_{SO} = 30$ meV, and the temperatures of the hot and the cold baths $T_h = 100$ K and $T_c = 30$ K, respectively.

processes. Isothermal processes transform the system through the phase transition point. TPT of Sn is associated with the band closing and hence we may expect similar signatures of TPT in a similar cycle considered in Ref. [24]. The cycle can be compared to that of an idealized Stirling cycle without regenerator. We will call the cycle in Ref. [24] as Stirling cycle. In the case of Sn the isomagnetic stages are replaced by the isoelectric processes as shown in Fig. 7. However, the energy level structure of Sn is different than the model (interacting spins) in Ref. [24]. At the K point, Sn can be considered as a four-level system (see Eq. (A1) in Appendix A). The only levels crossing are the two middle ones (lowest conduction and highest valence levels). We will first consider a direct application of the cycle in Ref. [24] to the full four-level Sn model then examine another case where a voltage bias is assumed to get a two-level model. We find that only the two-level model carries the signatures of TPT.

The heat exchanged between the system and its surroundings in each stage of the cycle are given by

$$\begin{aligned} Q_{BA} &= T_h(S(B) - S(A)), \quad Q_{CB} = U(C) - U(B), \quad (9) \\ Q_{DC} &= T_c(S(D) - S(C)), \quad Q_{AD} = U(A) - U(D), \quad (10) \end{aligned}$$

where

$$U(\alpha) = -\frac{\partial}{\partial \beta_i} \ln(Z(\alpha))|_{\varepsilon} \quad (11)$$

are the internal energies at constant electric field at each point $\alpha = A, B, C, D$ in the cycle and

$$S(\alpha) = k_B \ln(Z(\alpha)) + \frac{U(\alpha)}{T_i} \quad (12)$$

are the respective entropies given in terms of the internal energies. The total work produced during this cycle is given by

$$W_S = Q_{AB} + Q_{BC} + Q_{CD} + Q_{DA}. \quad (13)$$

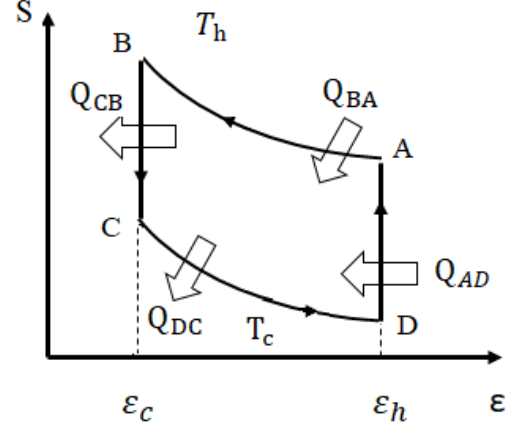


Figure 7. Entropy-Electric field graph of a Stirling cycle consisting of two isothermal and two isoelectric stages. During the isothermal process from A to B (C to D), the system is brought into contact with a heat bath at temperature T_h (T_c) and Q_{BA} (Q_{DC}) amount of heat absorbed (released). In the isoelectric processes, the external electric field decreases (increases) from ε_h (ε_c) to ε_c (ε_h) and the exchanged heat is Q_{CB} (Q_{AD}).

Plugging Eqs. (9) and (10), the total work is obtained in terms of the partition functions $Z(\alpha)$:

$$\begin{aligned} W_S &= k_B T_h \ln(Z(B)) - k_B T_h \ln(Z(A)) + k_B T_c \ln(Z(D)) \\ &\quad - k_B T_c \ln(Z(C)). \end{aligned} \quad (14)$$

We consider low energy band structures at room and low temperature for the following cases: (I) Without bias voltage and (II) With bias voltage.

1. Case (I): Without bias voltage

In this case we directly employ the cycle to the Sn with 4-level model at the K point (see Eq. (A1) in Appendix A). An explicit expression for work W_{S4} is derived in Appendix B. Setting $\varepsilon_h = 50$ meV, $\lambda_{SO} = 30$ meV, we let ε_c change from 0 to 50 meV. The temperatures of the hot and cold baths are $T_h = 400$ K and $T_c = 300$ K, respectively. Fig. 9 and Fig. 8b plot the net work and the efficiency of the cycle. They smoothly drop to zero as ε_c approaches to ε_h . There is no sign of TPT in this case.

When low temperatures are considered, or when we change λ_{SO} this behavior does not change. Hence we conclude that Stirling cycle does not yield any signatures of TPT for the full four-level Sn working substance.

2. Case (II): With bias voltage

In this case we consider application of a voltage bias, as proposed in Ref. [11], to restrict the number of levels in the Sn model to two electronic levels at the K point above

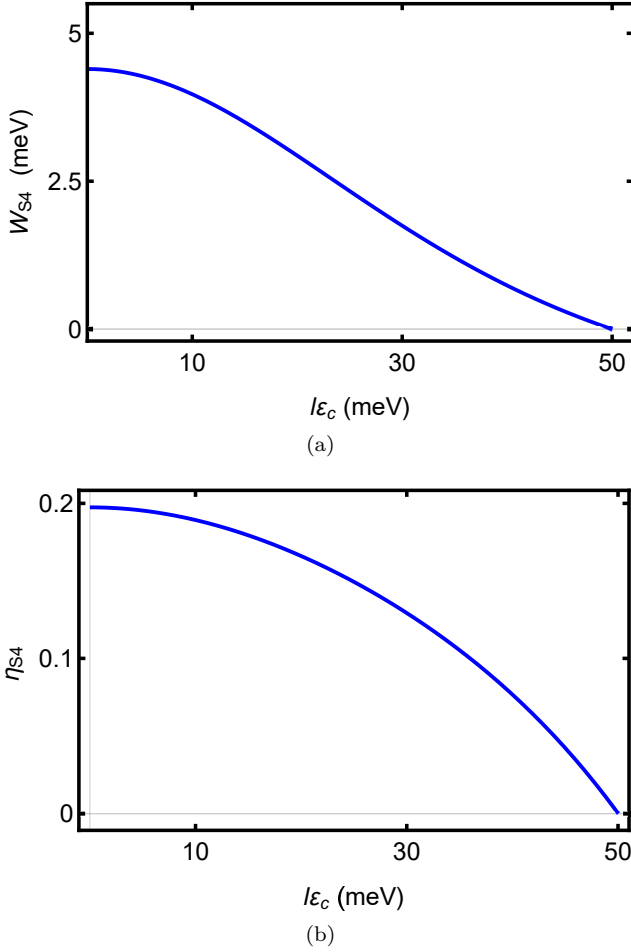


Figure 8. (Color Online)(a) Work W_{S4} and (b) Efficiency η_{S4} as a function of the electric potential at the cold isochore $l\epsilon_c$ for four-level Sn model under Stirling cycle for the electric potential at the hot isochore $l\epsilon_h = 50$ meV, and for the spin-orbit coupling strength $\lambda_{SO} = 30$ meV. Hot and cold baths are at temperatures $T_h = 400$ K and $T_c = 300$ K.

the Fermi level. The explicit expression of work W_{S2} for this effective two-level system is given in Appendix B. We plot W_{S2} and the efficiency η_{S2} with respect to $l\epsilon_c$ for different values of λ_{SO} in Fig. 9a and Fig. 9b, respectively. The positive work is produced with finite efficiency when $l\epsilon_c < \lambda_{SO}$. Work and efficiency increases with the SO coupling. This behavior is the same at low temperatures, too. If we fix $l\epsilon_c$ and plot the work with respect to $l\epsilon_h$, the positive work region becomes $l\epsilon_h > \lambda_{SO}$. Hence, we conclude that clear signature of TPT of Sn is found in Stirling cycle under voltage bias when Sn is in trivial insulator phase in one isochoric stage and in topological insulator phase in the other isochoric stage. Both four-level Sn in Otto cycle and two-level Sn in Stirling cycle exhibit clear signatures of TPT, however we remark that there is no gap closing in the upper pair of electronic levels and hence the influence of TPT in the two-level Sn on the work and efficiency is not as direct as in the four-level Sn.

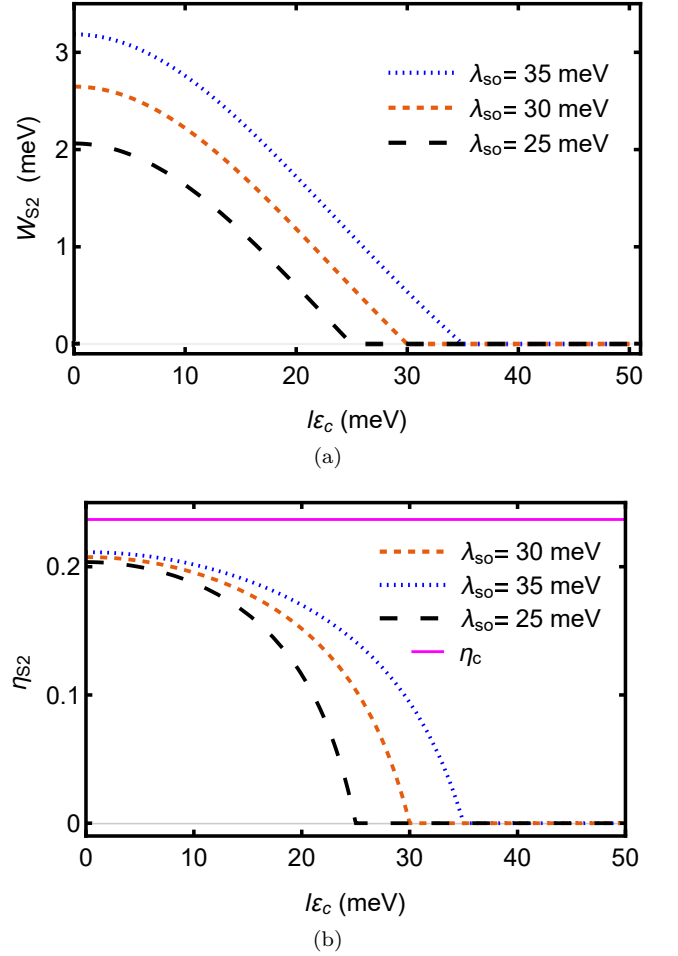


Figure 9. (Color Online)(a) Work W_{S2} and (b) Efficiency η_{S2} , of two-level Sn model under Stirling cycle, as a function of the electric potential at the cold isochore $l\epsilon_c$ for different spin-orbit coupling λ_{SO} . Hot and cold baths are at temperatures $T_h = 400$ K and $T_c = 300$ K and the electric potential at the hot isochore is $l\epsilon_h = 50$ meV. Upper solid line shows the Carnot efficiency η_C .

IV. IMPLEMENTATIONS OF THE THERMODYNAMIC CYCLES WITH TOPOLOGICAL INSULATORS

In addition to Sn (or Germanene or Silicene) as the working substance, the basic ingredients needed to construct a room temperature quantum heat engine with a TPT are tunable hot and cold baths that would be periodically in contact with the monolayer TI and tunable electric field that will vary between two values above and below the critical point. There are experimental reports on the successful fabrication of such monolayer TIs [42–45]. The effect of an external electric field on them has been studied in both theoretical and experimental works [35, 36]. While one may directly use the environment (room) temperature, more controllable environments can also be envisioned for monolayer TIs. For example, we may propose that a graphene bilayer can

be used as a scaffold for Sn. Such a set up preserves the topological properties of stanene and moreover, these stacked layers are stable above room temperature [35, 36]. Graphene has already been studied for its significant potential for heat flow control and energy harvesting [35, 36]; and there are investigations which deal with annealing graphene [35, 36]. Accordingly, graphene bilayer scaffold could be used to conduct heat in a controllable manner and can act as a tunable act as the hot and cold bath to implement the isothermal or isochoric heating and cooling stages of the cycles we consider.

V. CONCLUSIONS

We have investigated signatures of the topological phase transition (TPT) of a monolayer Stanene (Sn) under an applied electric field in the work and efficiency of thermodynamic engine cycles using the Sn as their working substance. We specifically considered an Otto cycle and a Stirling cycle. In the case of Otto cycle, positive work domain in the electric field space, as well as the magnitude of the work and efficiency, exhibit qualitative effects of TPT. A kink separates a double-peaked work output profile at the critical point of TPT. In the case of Stirling cycle, TPT has no signature unless a voltage bias is introduced to limit the involved levels to the electronic manifold. Under the voltage bias, there is no positive work output after the critical point, which is consistent with the conclusion in the Ref. [24]. This result generalizes the idea of the Ref. [24], which is using heat engine cycles to probe ordinary quantum phase transitions (QPTs) to the probing topological QPTs. Our method can also be an alternative to the typical scheme of probing TPT by the determination of the work distribution under a sudden quench. Our results are applicable to other monolayer topological insulators, such as Germanene and Silicene. The advantage of large spin-orbit coupling in such materials, relative to recently proposed Graphene flake heat engines [11], is to enhance the work and efficiency with SO coupling and room or higher temperature operation. We hope our results could inspire further studies of topological quantum heat engines.

ACKNOWLEDGEMENTS

We acknowledge support by the Scientific and Technological Research Council of Turkey (TÜBİTAK), Grant No. (117F097) and by the EU-COST Action (CA16221).

Appendix A: Work Expression for Quantum Otto Cycle

At $k = 0$, Eq. (4) yields four distinct energy levels:

$$\begin{aligned} E_1^i &= |\ell\varepsilon_i - \lambda_{\text{SO}}|, & E_2^i &= -|\ell\varepsilon_i - \lambda_{\text{SO}}|, \\ E_3^i &= \ell\varepsilon_i + \lambda_{\text{SO}}, & E_4^i &= -(\ell\varepsilon_i + \lambda_{\text{SO}}), \end{aligned} \quad (\text{A1})$$

with $i = h, c$. Hence, we are dealing with a four level system, where there are two conduction and two valence levels. Each level is four-fold degenerate due to the valley (η) and spin (s) quantum numbers in Eq. (4) so that the degeneracy factor becomes $g(E_n^i) = 4$, where $n = 1, \dots, 4$. The partition function for a stanene sheet in contact with a thermal bath at temperature T is then given by

$$\begin{aligned} Z_i &= g(E_n^i) \sum_{n=1}^4 e^{-\beta E_n^i} \\ &= 8[\cosh(\beta|\ell\varepsilon_i - \lambda_{\text{SO}}|) + \cosh(\beta(\ell\varepsilon_i + \lambda_{\text{SO}}))], \end{aligned} \quad (\text{A2})$$

with $i = h, c$.

The heat received Q_{in} and ejected Q_{out} , are then obtained as

$$\begin{aligned} Q_{\text{in}} &= 2(|\ell\varepsilon_h - \lambda_{\text{SO}}|) \times \\ &\quad \left(\frac{\sinh(\beta_c|\ell\varepsilon_c - \lambda_{\text{SO}}|)}{Z_c} - \frac{\sinh(\beta_h|\ell\varepsilon_h - \lambda_{\text{SO}}|)}{Z_h} \right) \\ &\quad + 2(\ell\varepsilon_h + \lambda_{\text{SO}}) \times \\ &\quad \left(\frac{\sinh(\beta_c(\ell\varepsilon_c + \lambda_{\text{SO}}))}{Z_c} - \frac{\sinh(\beta_h(\ell\varepsilon_h + \lambda_{\text{SO}}))}{Z_h} \right), \end{aligned} \quad (\text{A3})$$

and

$$\begin{aligned} Q_{\text{out}} &= \sum_{n=1}^4 E_n^c (P_n(T_h) - P_n(T_c)) \\ &= 2(|\ell\varepsilon_c - \lambda_{\text{SO}}|) \times \\ &\quad \left(\frac{\sinh(\beta_c|\ell\varepsilon_c - \lambda_{\text{SO}}|)}{Z_c} - \frac{\sinh(\beta_h|\ell\varepsilon_h - \lambda_{\text{SO}}|)}{Z_h} \right) \\ &\quad + 2(\ell\varepsilon_c + \lambda_{\text{SO}}) \times \\ &\quad \left(\frac{\sinh(\beta_c(\ell\varepsilon_c + \lambda_{\text{SO}}))}{Z_c} - \frac{\sinh(\beta_h(\ell\varepsilon_h + \lambda_{\text{SO}}))}{Z_h} \right), \end{aligned} \quad (\text{A4})$$

respectively. By using Eq. (A3) and Eq. (A4) in Eq. (7), we arrive at the explicit expression for work given in Eq. (8).

Appendix B: Work Expression for Stirling Cycle

When we consider all four levels of one-particle stanene system, the partition functions at each point in the isothermal-isoelectric cycle described in Sec. IIIB are

given by Eq. (A2) as

$$\begin{aligned} Z_{S4}(A) &= 8(\cosh(\beta_h |l\varepsilon_h - \lambda_{SO}|) + \cosh(\beta_h (l\varepsilon_h + \lambda_{SO}))), \\ Z_{S4}(B) &= 8(\cosh(\beta_h |l\varepsilon_c - \lambda_{SO}|) + \cosh(\beta_h (l\varepsilon_c + \lambda_{SO}))), \\ Z_{S4}(C) &= 8(\cosh(\beta_c |l\varepsilon_c - \lambda_{SO}|) + \cosh(\beta_c (l\varepsilon_c + \lambda_{SO}))), \\ Z_{S4}(D) &= 8(\cosh(\beta_c |l\varepsilon_h - \lambda_{SO}|) + \cosh(\beta_c (l\varepsilon_h + \lambda_{SO}))). \end{aligned} \quad (B1)$$

Using Eqs. (B1) and Eq. (14), the explicit expression for work for four bands is obtained as

$$\begin{aligned} W_{S4} = & -\frac{\ln(\cosh(\beta_c |l\varepsilon_c - \lambda_{SO}|) + \cosh(\beta_c (l\varepsilon_c + \lambda_{SO})))}{\beta_c} \\ & + \frac{\ln(\cosh(\beta_c |l\varepsilon_h - \lambda_{SO}|) + \cosh(\beta_c (l\varepsilon_h + \lambda_{SO})))}{\beta_c} \\ & + \frac{\ln(\cosh(\beta_h |l\varepsilon_c - \lambda_{SO}|) + \cosh(\beta_h (l\varepsilon_c + \lambda_{SO})))}{\beta_h} \\ & - \frac{\ln(\cosh(\beta_h |l\varepsilon_h - \lambda_{SO}|) + \cosh(\beta_h (l\varepsilon_h + \lambda_{SO})))}{\beta_h} \end{aligned} \quad (B2)$$

The partition function for the two-level system is given by

$$Z_{S2} = 4e^{\beta |l\varepsilon - \lambda_{SO}|} + 4e^{\beta (l\varepsilon + \lambda_{SO})} \quad (B3)$$

Using Eq. (B3) to calculate the partition function for the each point in the cycle and once again using Eq. (14), the explicit expression for work for the effectively two-level system is obtained as

$$\begin{aligned} W_{S2} = & -\frac{1}{\beta_c} \ln(e^{\beta_c |l\varepsilon_c - \lambda_{SO}|} + e^{\beta_c (l\varepsilon_c + \lambda_{SO})}) \\ & + \frac{1}{\beta_c} \ln(e^{\beta_c |l\varepsilon_h - \lambda_{SO}|} + e^{\beta_c (l\varepsilon_h + \lambda_{SO})}) \\ & + \frac{1}{\beta_h} \ln(e^{\beta_h |l\varepsilon_c - \lambda_{SO}|} + e^{\beta_h (l\varepsilon_c + \lambda_{SO})}) \\ & - \frac{1}{\beta_h} \ln(e^{\beta_h |l\varepsilon_h - \lambda_{SO}|} + e^{\beta_h (l\varepsilon_h + \lambda_{SO})}) \end{aligned} \quad (B4)$$

-
- [1] D. S. L. Cardwell, “From watt to clausius: The rise of thermodynamics in the early industrial age.” *The Library Quarterly* **43**, 168–169 (1973).
 - [2] H. E. D. Scovil and E. O. Schulz-DuBois, “Three-Level Masers as Heat Engines,” *Phys. Rev. Lett.* **2**, 262–263 (1959).
 - [3] M. O. Scully, M. S. Zubairy, G. S. Agarwal, and H. Walther, “Extracting Work from a Single Heat Bath via Vanishing Quantum Coherence,” *Science* **299**, 862–864 (2003).
 - [4] C. A. Ryan, O. Moussa, J. Baugh, and R. Laflamme, “Spin Based Heat Engine: Demonstration of Multiple Rounds of Algorithmic Cooling,” *Phys. Rev. Lett.* **100**, 140501 (2008).
 - [5] Johannes Roßnagel, Samuel T. Dawkins, Karl N. Tolazzi, Obinna Abah, Eric Lutz, Ferdinand Schmidt-Kaler, and Kilian Singer, “A single-atom heat engine,” *Science* **352**, 325–329 (2016).
 - [6] Ali Ü. C. Hardal and Özgür E. Müstecaplıoğlu, “Superradiant Quantum Heat Engine,” *Scientific Reports* **5**, 12953 (2015).
 - [7] Keye Zhang, Francesco Bariani, and Pierre Meystre, “Quantum Optomechanical Heat Engine,” *Phys. Rev. Lett.* **112**, 150602 (2014).
 - [8] Ali Ü. C. Hardal, Nur Aslan, C. M. Wilson, and Özgür E. Müstecaplıoğlu, “Quantum heat engine with coupled superconducting resonators,” *Phys. Rev. E* **96**, 062120 (2017).
 - [9] Francisco J. Peña, Michel Ferré, P. A. Orellana, René G. Rojas, and P. Vargas, “Optimization of a relativistic quantum mechanical engine,” *Phys. Rev. E* **94**, 022109 (2016).
 - [10] Enrique Muñoz and Francisco J. Peña, “Quantum heat engine in the relativistic limit: The case of a Dirac particle,” *Phys. Rev. E* **86**, 061108 (2012).
 - [11] Francisco J. Peña and Enrique Muñoz, “Magnetostrain-driven quantum engine on a graphene flake,” *Phys. Rev. E* **91**, 052152 (2015).
 - [12] Enrique Muñoz, Francisco J. Peña, and Alejandro González, “Magnetically-Driven Quantum Heat Engines: The Quasi-Static Limit of Their Efficiency,” *Entropy* **18**, 173 (2016).
 - [13] Arjun Mani and Colin Benjamin, “Strained-graphene-based highly efficient quantum heat engine operating at maximum power,” *Phys Rev E* **96**, 032118 (2017).
 - [14] Clifford V Johnson, “Holographic heat engines,” *Class. Quantum Grav.* **31**, 205002 (2014).
 - [15] Jean-Philippe Brantut, Charles Grenier, Jakob Meineke, David Stadler, Sebastian Krinner, Corinna Kollath, Tilman Esslinger, and Antoine Georges, “A Thermoelectric Heat Engine with Ultracold Atoms,” *Science* **342**, 713–715 (2013).
 - [16] H. T. Quan, Yu-xi Liu, C. P. Sun, and Franco Nori, “Quantum thermodynamic cycles and quantum heat engines,” *Phys. Rev. E* **76**, 031105 (2007).
 - [17] Giuliano Benenti, Giulio Casati, Keiji Saito, and Robert S. Whitney, “Fundamental aspects of steady-state conversion of heat to work at the nanoscale,” *Phys. Rep.* **694**, 1–124 (2017).
 - [18] Robert Alicki and Ronnie Kosloff, “Introduction to Quantum Thermodynamics: History and Prospects,” (2018), [arXiv:1801.08314 \[quant-ph\]](https://arxiv.org/abs/1801.08314).
 - [19] Sai Vinjanampathy and Janet Anders, “Quantum thermodynamics,” *Contemp. Phys.* **57**, 545–579 (2016).
 - [20] John Goold, Marcus Huber, Arnau Riera, Lúcia del Río, and Paul Skrzypczyk, “The role of quantum information in thermodynamics—a topical review,” *J. Phys. A: Math. Theor* **49**, 143001 (2016).
 - [21] James Klatzow, Jonas N. Becker, Patrick M. Ledingham, Christian Weinzetl, Krzysztof T. Kaczmarek, Dylan J. Saunders, Joshua Nunn, Ian A. Walmsley, Raam Uzdin, and Eilon Poem, “Experimental demonstration of quan-

- tum effects in the operation of microscopic heat engines,” (2017), [arXiv:1710.08716](#).
- [22] Yueyang Zou, Yue Jiang, Yefeng Mei, Xianxin Guo, and Shengwang Du, “Quantum Heat Engine Using Electromagnetically Induced Transparency,” *Phys. Rev. Lett.* **119**, 050602 (2017).
 - [23] Michele Campisi and Rosario Fazio, “The power of a critical heat engine,” *Nat. Commun.* **7**, 11895 (2016).
 - [24] Yu-Han Ma, Shan-He Su, and Chang-Pu Sun, “Quantum thermodynamic cycle with quantum phase transition,” *Phys. Rev. E* **96**, 022143 (2017).
 - [25] E. Mascarenhas, H. Bragança, R. Dorner, M. França Santos, V. Vedral, K. Modi, and J. Goold, “Work and quantum phase transitions: Quantum latency,” *Phys. Rev. E* **89**, 062103 (2014).
 - [26] Alessandro Silva, “Statistics of the Work Done on a Quantum Critical System by Quenching a Control Parameter,” *Phys. Rev. Lett.* **101**, 120603 (2008).
 - [27] Yong Xu, Peizhe Tang, and Shou-Cheng Zhang, “Large-gap quantum spin Hall states in decorated stanene grown on a substrate,” *Phys. Rev. B* **92**, 081112 (2015).
 - [28] Yong Xu, Binghai Yan, Hai-Jun Zhang, Jing Wang, Gang Xu, Peizhe Tang, Wenhui Duan, and Shou-Cheng Zhang, “Large-Gap Quantum Spin Hall Insulators in Tin Films,” *Phys. Rev. Lett.* **111**, 136804 (2013).
 - [29] Motohiko Ezawa, “A topological insulator and helical zero mode in silicene under an inhomogeneous electric field,” *New J. Phys.* **14**, 033003 (2012).
 - [30] S. Cahangirov, M. Topsakal, E. Aktürk, H. Şahin, and S. Ciraci, “Two- and One-Dimensional Honeycomb Structures of Silicon and Germanium,” *Phys. Rev. Lett.* **102**, 236804 (2009).
 - [31] Cheng-Cheng Liu, Hua Jiang, and Yugui Yao, “Low-energy effective Hamiltonian involving spin-orbit coupling in silicene and two-dimensional germanium and tin,” *Phys. Rev. B* **84**, 195430 (2011).
 - [32] M. Fadaie, N. Shahtahmassebi, M.R. Roknabad, and O. Gulseren, “Investigation of new two-dimensional materials derived from stanene,” *Comp. Mater. Sci.* **137**, 208–214 (2017).
 - [33] Michel Houssa, Bas van den Broek, Konstantina Iordanidou, Anh Khoa Augustin Lu, Geoffrey Pourtois, Jean-Pierre Locquet, Valery Afanas’ev, and André Stesmans, “Topological to trivial insulating phase transition in stanene,” *Nano Res.* **9**, 774–778 (2016).
 - [34] M. Fadaie, N. Shahtahmassebi, and M. R. Roknabad, “Effect of external electric field on the electronic structure and optical properties of stanene,” *Opt. Quant. Electron* **48** (2016), 10.1007/s11082-016-0709-5.
 - [35] Shuichi Murakami, “Gap closing and universal phase diagrams in topological insulators,” *Physica E* **43**, 748–754 (2011).
 - [36] J. E. Moore and L. Balents, “Topological invariants of time-reversal-invariant band structures,” *Phys. Rev. B* **75**, 121306 (2007).
 - [37] Feng-feng Zhu, Wei-jiong Chen, Yong Xu, Chun-lei Gao, Dan-dan Guan, Can-hua Liu, Dong Qian, Shou-Cheng Zhang, and Jin-feng Jia, “Epitaxial growth of two-dimensional stanene,” *Nat. Mater.* **14**, 1020–1025 (2015).
 - [38] Yong Xu, Zhongxue Gan, and Shou-Cheng Zhang, “Enhanced Thermoelectric Performance and Anomalous Seebeck Effects in Topological Insulators,” *Phys. Rev. Lett.* **112**, 226801 (2014).
 - [39] Paolo Mognini, Evert van Nieuwenburg, and R. Chitra, “Sensing Floquet-Majorana fermions via heat transfer,” *Phys. Rev. B* **96**, 125144 (2017).
 - [40] Motohiko Ezawa, “Monolayer Topological Insulators: Silicene, Germanene, and Stanene,” *Journal of the Physical Society of Japan* **84**, 121003 (2015).
 - [41] M. V. Berry, “Transitionless quantum driving,” *J. Phys. A: Math. Theor.* **42**, 365303 (2009).
 - [42] Guanhua Zhang, Huajun Qin, Jun Chen, Xiaoyue He, Li Lu, Yongqing Li, and Kehui Wu, “Growth of Topological Insulator Bi₂Se₃ Thin Films on SrTiO₃ with Large Tunability in Chemical Potential,” *Adv. Funct. Mater.* **21**, 2351–2355 (2011).
 - [43] Can-Li Song, Yi-Lin Wang, Ye-Ping Jiang, Yi Zhang, Cui-Zu Chang, Lili Wang, Ke He, Xi Chen, Jin-Feng Jia, Yayu Wang, Zhong Fang, Xi Dai, Xin-Cheng Xie, Xiaoliang Qi, Shou-Cheng Zhang, Qi-Kun Xue, and Xucun Ma, “Topological insulator Bi₂Se₃ thin films grown on double-layer graphene by molecular beam epitaxy,” *Appl. Phys. Lett.* **97**, 143118 (2010).
 - [44] Namrata Bansal, Yong Seung Kim, Eliav Edrey, Matthew Brahlek, Yoichi Horibe, Keiko Iida, Makoto Tanimura, Guo-Hong Li, Tian Feng, Hang-Dong Lee, Torgny Gustafsson, Eva Andrei, and Seongshik Oh, “Epitaxial growth of topological insulator Bi₂Se₃ film on Si(111) with atomically sharp interface,” *Thin Solid Films* **520**, 224–229 (2011).
 - [45] Xi Chen, Xu-Cun Ma, Ke He, Jin-Feng Jia, and Qi-Kun Xue, “Molecular Beam Epitaxial Growth of Topological Insulators,” *Adv. Mater.* **23**, 1162–1165 (2011).